Desalination and Water Treatment
www.deswater.com
doi: 10.5004/dwt.2019.24762

171 (2019) 183–195
December

Enhanced adsorption of Pb(II) from aqueous solution by magnesium-incorporated hydroxyapatite with poor crystalline structure

Min Zhou[a,*], Xinlong Yan[a], Hong Zou[b], Yaqin Zhao[b], Ningning Yin[b], Can Zhang[b], Liping Wang[b]

[a]*School of Chemical Engineering & Technology, China University of Mining & Technology, Xuzhou 221116, China, Tel./Fax:+86 516 83590163; email: zm@cumt.edu.cn (M. Zhou)*
[b]*School of Environment and Spatial Informatics, China University of Mining & Technology, Xuzhou 221116, China*

Received 2 April 2019; Accepted 31 July 2019

ABSTRACT

In this work, magnesium-incorporated hydroxyapatite (MHAP), with a poor crystalline structure was synthesized using a sol-gel method to remove lead from aqueous solutions. The results show that the adsorption capacity of MHAP for lead greatly increased compared with that of hydroxyapatite, which exhibits an adsorption capacity of 227.1 mg g^{-1} at an initial lead concentration of 550 mg L^{-1} at 30°C. This capacity is higher than that of previously reported hydroxyapatite-related adsorbents. In addition, the adsorption isotherm could be better described by a Langmuir isotherm, and the adsorption kinetics conformed to the pseudo-second-order model. The MHAP removes lead via dissolution–precipitation reaction. During the adsorption process, the MHAP was converted to hydroxyapatite [$(Pb_{10}(PO_4)_6(OH)_2)$ or $(Pb_5(PO_4)_3OH)$] as well as calcium lead phosphate hydroxide $(Ca_2Pb_8(PO_4)_6(OH)_2$ and lead phosphate $(Pb_9(PO_4)_6)$.

Keywords: Magnesium-incorporated hydroxyapatite; Adsorption; Lead; Lead phosphate hydroxide

1. Introduction

Lead, which is widely found in the natural environment, is generally applied in the metallurgical, paint and cosmetic manufacturing industrial fields [1,2]. Lead is regarded as a significant pollutant in wastewater, waste gas and soil [3] and is even considered to be a "possible human carcinogen" by the US Environmental Protection Agency (EPA) due to its long-term accumulation in the food chain, non-degradable nature in the environment and toxicity to life [4]. In recent years, a serious phenomenon occurred in China in which lead levels in the blood of children in rural areas exceeded 100 μg L^{-1}, which indicated that the ecological environment was damaged and that human beings suffered from lead pollution [5,6]. Therefore, developing a method to efficiently remove lead from water and soil is urgent.

The physical chemistry methods that are commonly used to remove lead in aqueous solutions include precipitation, membrane separation, electrochemical techniques, solvent extraction, filtration and adsorption [7]. Among all of the proposed approaches, adsorption has aroused great interest because of its low cost and relatively simple process [8]. Hydroxyapatite (HAP, $Ca_5(PO_4)_3OH$), which is derived from phosphatic rocks [9], is a common mineral adsorbent because of its extensive availability, chemical stability across a wide range of natural conditions, and ability to immobilize harmful metal ions [10,11]. HAP has been demonstrated to have removal abilities for Pd^{2+}, Cd^{2+}, Cu^{2+}, Zn^{2+}, Ni^{2+} and other metal ions [12–15]. However, the low number of functional groups and weak affinity for contaminants of HAP limit its applications.

* Corresponding author.

Hashimoto and Sato [12] reported that poorly crystalline HAP has a better adsorption capacity for heavy metals compared with commercial, pure HAP. These results were also confirmed by Fernane et al. [13]. In addition, doping cationic or anionic molecules into HAP was demonstrated to be an effective way to break the lattice and improve its properties. The mechanical properties of HAP were improved by doping with iron or zinc. In addition, aluminum-modified HAP and sulfate-doped HAP were found to have a higher de-fluoridation capacity [16–19]. Considering the similar chemical properties and smaller ionic radius of magnesium compared with that of calcium in HAP, magnesium-incorporated HAP should more easily facilitate substitution with heavy metal ions. Thus, combining the merits of magnesium doping and poor-crystallinity HAP may enhance its adsorption capacity for heavy metals.

On the other hand, Suzuki et al. [20] suggested that the adsorption of lead by HAP is an ion exchange process. Lead was fixed as an insoluble phosphate, and calcium ions are released into the aqueous solution [13,21]. This hypothesis was revised by Ma et al. [22], and Xu and Schwartz [23] who proposed that the dissolution of HAP and the subsequent precipitation of pyromorphite were responsible for the immobilization of Pb^{2+}. Additionally, Mavropoulos et al. [24] reported that surface complexation could also be involved in the immobilization of Pb^{2+}. It is well known that surface functional groups are important for adsorption. However, the reaction relationship between $PO_4^{3-}$and –OH on the HAP surface and Pb^{2+} is poorly understood.

Thus, in this work, magnesium-incorporated HAP with a poor-crystallinity was synthesized and characterized, and its adsorption properties for lead removal were investigated. Besides, the mechanism of lead adsorption on the as-synthesized adsorbent was studied.

2. Materials and methods

2.1. Materials

All chemicals were of analytical grade and were used as received without any further purification. Calcium nitrate ($Ca(NO_3)_2{\cdot}4H_2O$, 99%), phosphoric acid (H_3PO_4, ≥85 wt. %), magnesium nitrate ($Mg(NO_3)_2{\cdot}6H_2O$, >99%), lead nitrate ($Pb(NO_3)_2$, ≥99.0%), ammonia solution ($NH_3{\cdot}H_2O$, 25%–28%) and nitric acid (HNO_3, 65%–68%) were obtained from Nanjing Chemical Reagent Co., China. Deionized water was used for all the experiments.

2.2. Synthesis of the adsorbents

The pure and magnesium-modified HAP were synthesized using a sol-gel method. Typically, mixed solutions of $Ca(NO_3)_2$ (0.5 M) and $Mg(NO_3)_2$ (0.5 M) with Mg/Ca molar ratios of 0, 0.25, 0.5, 0.75 and 1 were added to different flat-bottom flasks and followed by the addition of 120 mL of 1 M H_3PO_4. Then, the flasks were placed onto a magnetic stirring heating plate, and the temperature of the solutions was maintained at 30°C. Subsequently, the pH value of the solutions was adjusted to 10 with continuous stirring until the formation of a white gel. The resulting gel was stirred for another 0.5 h. After that, the flasks were placed in a water bath at 70°C for 24 h, and subsequently, the white gel was separated from the solution through filtration and washed three times with deionized water. The solid product was then obtained after dried at 90°C for 12 h and calcined at 300°C for 2 h.

The synthetic samples, after grinding and sieving, were designated as HAP, 0.25 MHAP, 0.5 MHAP, 0.75 MHAP and MHAP, respectively, and were stored in a closed drying vessel.

2.3. Characterization of the adsorbents

The surface morphology and structure of the adsorbents were examined using scanning electron microscopy (SEM, FEI Quanta TM 250, USA). The infrared spectra were obtained from a Bruker (Germany) Vertex 80 Fourier transform infrared spectrometer (FT-IR), and the spectra were recorded from 4,000 to 400 cm^{-1} at a resolution of 0.06 cm^{-1}. The powder X-ray diffraction (XRD) of the adsorbents was conducted with a Bruker (Germany) D8 advanced X-ray diffractometer that operated with Cu Kα radiation at 40 kV and 30 mA. X-ray photoelectron spectroscopy (XPS) was performed on a Thermo Fisher (USA) ESCALAB 250Xi with energy steps of 1 eV (for the survey spectrum) and 0.5 eV (for the high-resolution spectra for each element peak). N_2 adsorption–desorption isotherms were measured on a Micromeritics (USA) ASAP 2460 porosimeter after degassing the sample overnight at 100°C. Total pore volume was determined by the volume of liquid nitrogen adsorbed at a relative pressure of 0.99. Average pore diameter was calculated as 4 V/A (V: pore volume; A: surface area).

2.4. Adsorption experiments

The adsorption experiments were performed in a series of 250 mL conical flasks. The HAP or MHAP (0.1 g) was placed into 50 mL of a lead solution with concentrations ranging from 50 to 550 mg L^{-1}. The suspensions were transferred to a constant temperature shaking table that operated at a speed of 180 rmp at 20°C–40°C for 4 h, which was sufficient to reach adsorption equilibrium. The supernatants were filtered through a 0.45 μm qualitative filter paper, and the concentrations of Pb^{2+}, Ca^{2+}, and Mg^{2+} in the filtrate were measured using an inductively coupled plasma optical emission spectrometer (ICP-OES). The filter residue was collected and dried at 50°C for further analysis.

The adsorption capacity (q_e, mg g^{-1}) was calculated according to the following equation:

$$q_e = \frac{(C_0 - C_e)V}{1{,}000m} \tag{1}$$

where C_0 and C_e are the initial and final lead concentrations (mg L^{-1}), respectively, V is the volume of the lead solution (mL) and m is the mass of the adsorbent (g).

The adsorption kinetic experiments were performed by adding 0.1 g of the as-prepared sample to a 250 mL Erlenmeyer flask filled with 50 mL of lead solution (200 or 500 mg/L). The flask was sealed and agitated at 30°C. The aqueous samples were taken out at pre-set time intervals,

and the concentrations of Pb^{2+} were similarly measured. The solution pH was adjusted with 0.5 M HNO_3 or 0.5 M NaOH aqueous solution to reach the desired pH values.

3. Results and discussion

3.1. Characterization of the adsorbents

The morphology of pure HAP and Mg-doped HAP with different Mg/Ca molar ratios was characterized using SEM (Fig. 1). The diameters of the HAP and 0.25 MHAP samples ranged from 50 to 200 μm with irregular square structures. As the Mg/Ca molar ratio increased to 0.5 and 0.75, the diameters of the particles decreased to 20–50 μm and 8–25 μm, respectively. Notably, the particle size of MHAP decreased significantly (to 5–15 μm) with a further increase of the Mg/Ca molar ratio to 1. Compared with the other four adsorbents, the MHAP particles were smaller, thinner, and more dispersible with a more amorphous morphology.

The porosities of the samples were measured, and the results are compiled in Table 1. It was obvious that the surface area improved significantly through the addition of Mg.

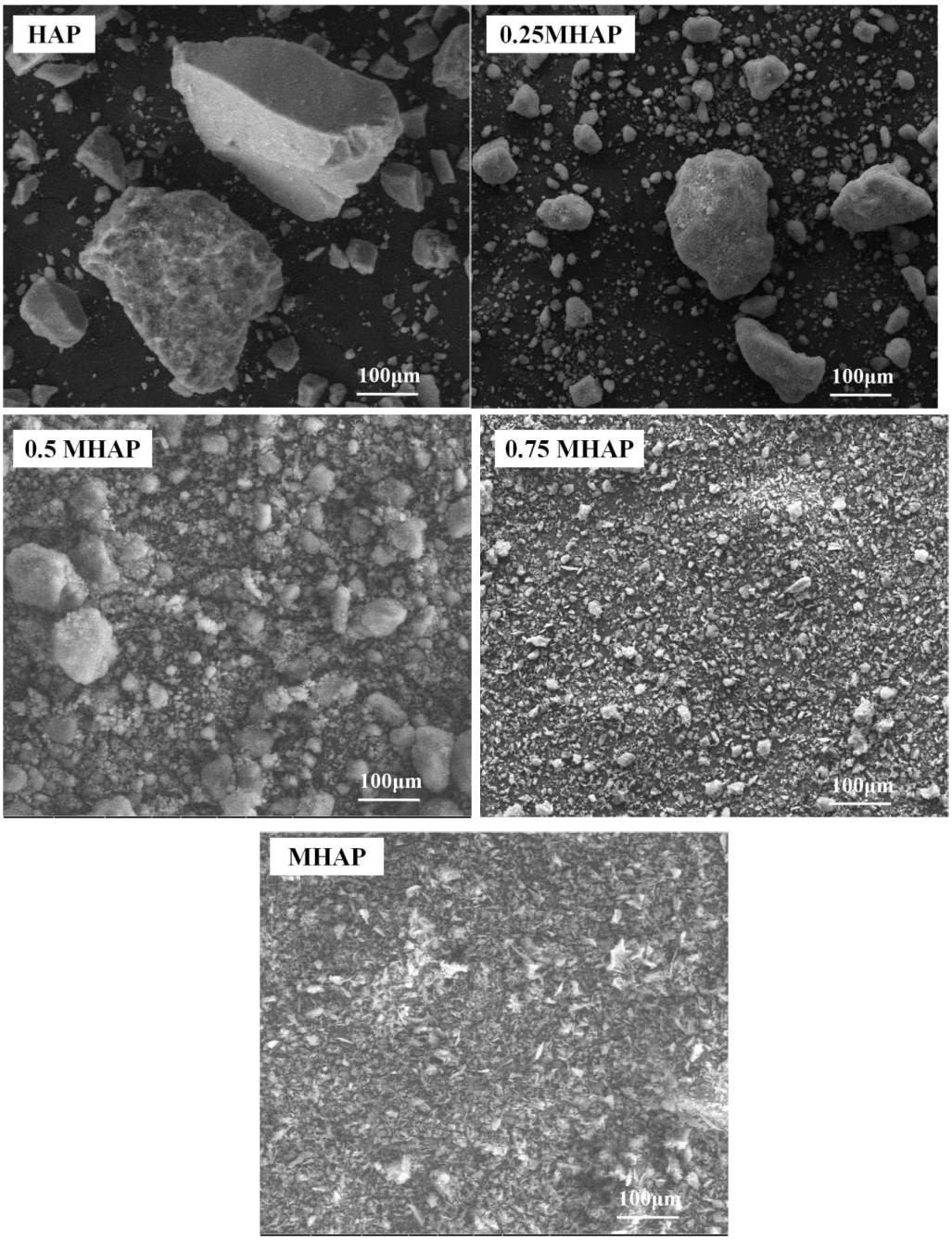

Fig. 1. SEM images of magnesium-incorporated HAP with different Mg/Ca atomic ratios.

Table 1
Surface area and porosity data of HAP and MHAPs

Samples	Pore volume/ (cm^3/g)	Particle size/nm	Surface area/(m^2/g)
HAP	0.12	31.72	22.77
0.25 MHAP	0.25	28.55	34.31
0.5 MHAP	0.24	26.11	37.12
0.75 MHAP	0.17	21.01	40.60
MHAP	0.34	25.46	50.72

The specific surface areas of HAP and MHAP were 22.77 and 50.72 m^2/g, respectively. This high surface area can be expected to enhance the adsorption performance.

The FT-IR spectra of the HAP and MHAPs are provided in Fig. S1. The peaks at 472, 570 and 604 cm^{-1} can be attributed to the bending vibration of P–O, and the peaks at 1,098 and 1,068 cm^{-1} resulted from the stretching vibration of P–O, which indicates the presence of PO_4^{3-} in all samples [25]. The peaks between 3,400 and 3,450 cm^{-1} belong to the band of –OH. The number of functional group can be estimated from the corresponding peak area. It was easily found that the peak areas at 570 to 470 cm^{-1}, 1,000 to 1,100 cm^{-1} and 3,400 to 3,450 cm^{-1} for the MHAPs were higher than those for HAP, which suggested that the doping of magnesium increases the number of functional groups of PO_4^{3-} and –OH on the sample surface. A new peak appears after doping with magnesium, and this peak likely reflects a bond that was formed by Mg and other ions. The peak at 1,640 cm^{-1} is ascribed to free water. The peak at 1,440 to 1,460 cm^{-1} can be ascribed to C–O bands, which may be due to the absorption of carbon dioxide in the air under alkaline conditions [26]. The stretching vibration peak of N–O appears at 1,383 to 1,385 cm^{-1}, which can be attributed to NO_3^- in the raw materials.

The XPS spectra of the five synthesized materials are shown in Fig. 2. The binding energies of the Ca2p, O1s and P2p peaks were 346.9, 530.9 and 132.8 eV, respectively, which agree with the values for hydroxyapatite [27–29]. It is clear that magnesium was successfully doped into the materials because the peak of Mg1s appeared. The binding energy of Mg1s was 1,304.8 eV, which approximately conformed to $MgX_2{\cdot}nH_2O$ as analyzed by the NIST X-ray Photoelectron Spectroscopy Database. The atomic ratio of each element on the outer surface of the synthesized adsorbents was also investigated using XPS. For the MHAPs, the measured contents of magnesium were 3.77%, 5.4%, 11.09% and 16.33%, respectively, with an increase in the Mg content from 0.25 to 1 in the samples. The atomic ratio of Mg/P or Ca/P was calculated from the ratio of the peak intensity. Generally, the Ca/P ratio of pure HAP was 1.67 [30], which was different than the results obtained here in which the Mg/P ratio of MHAP was 1.92 and the Ca/P ratio of HAP was 1.38. Compared with HAP, MHAP lacked phosphorus ions, which may possess more active sites [31,32]. The binding energy of O1s is about 530.9 eV, with the increase of Mg content in the samples, the contents of O increased. This may be because that the atomic weight of Mg is lower than that of Ca, thus, more O atom was combined per gram of sample.

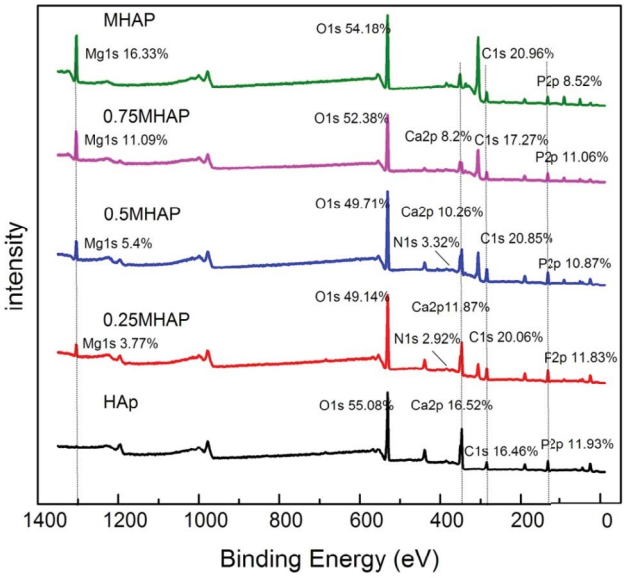

Fig. 2. XPS spectra of HAP, 0.25 MHAP, 0.5 MHAP, 0.75 MHAP and MHAP.

Fig. 3 shows the XRD patterns for the synthesized HAP and MHAPs. The diffraction peaks of HAP and 0.25 MHAP that were observed at 26°, 32°, 40°, 47° and 50° confirmed the formation of a hydroxyapatite structure [28]. Calcium hydrogen phosphate hydroxide ($Ca_9(HPO_4)(PO_4)_5OH$, PDF-46-0905) and magnesium whitlockite ($((Ca,Mg)_3(PO_4)_2$, PDF-13-0404) were also detected in the HAP and 0.25 MHAP samples. The main diffraction peaks were sharp and narrow, which indicated that the synthesized HAP possessed a good crystallinity. The peaks located at 17°, 21°, 28°, 34° and 45° in the pattern of the 0.25 MHAP sample can be attributed to calcium magnesium phosphate ($Ca_7Mg_2P_6O_{24}$, PDF-20-0348). With increasing the Mg/Ca molar ratio to be greater than 0.5, the main peaks of the crystalline phase disappeared, which indicated the formation of an amorphous phase. This may be because the lattice structure of HAP was destroyed with a high Mg incorporation [31–33]. Thus, this also indicates that a HAP adsorbent with poor crystallinity was successfully synthesized.

3.2. Adsorption experiments

The effect of the doping amount of Mg on the adsorption capacity of HAP for Pb^{2+} at different initial concentrations is presented in Fig. 4. The results showed that all adsorbents had a good removal capacity for aqueous Pb^{2+}. Clearly, with an increasing amount of incorporated Mg, the equilibrium adsorption capacity of the MHAPs improved greatly. The equilibrium adsorption capacities of HAP, 0.25 MHAP, 0.5 MHAP, 0.75 MHAP and MHAP were 71.0, 117.6, 169. 0, 197.0 and 218.0 mg g^{-1}, respectively. It can be clearly seen that the capacity of MHAP is almost three times larger than that of HAP and is twice as large as that of 0.25 MHAP. When the initial Pb^{2+} concentration was below 50 mg L^{-1}, the removal efficiency of all adsorbents was higher than 98.8%, as shown in Fig. S2. The results also indicated that magnesium ions

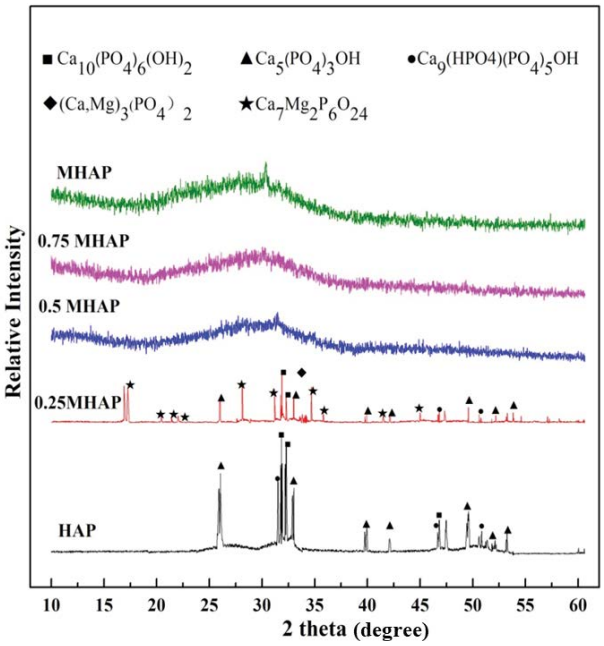

Fig. 3. X-ray diffraction patterns of HAP, 0.25 MHAP, 0.5 MHAP, 0.75 MHAP and MHAP.

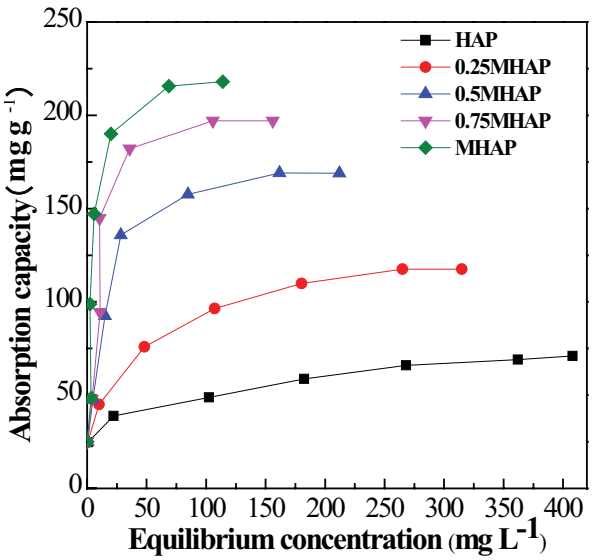

Fig. 4. Adsorption isotherm of Pb^{2+} ions onto HAP, 0.25 MHAP, 0.5 MHAP, 0.75 MHAP and MHAP.

could obviously improve the adsorption performance of HAP. In contrast to those previous reported adsorbents (Table 2), MHAP had a superior performance for the immobilization of lead.

The experimental data were modeled by the Langmuir and Freundlich isotherm models, and the two equations are presented in Eqs. (2) and (3).

$$\frac{C_e}{q_e} = \frac{1}{q_m K_L} + \frac{C_e}{q_m} \tag{2}$$

$$\ln q_e = \frac{1}{n}\ln C_e + \ln k_F \tag{3}$$

where q_m is the maximum saturated monolayer adsorption capacity and b is the Langmuir constant. K_F is the Freundlich constant and n is the degree of favorability of adsorption. C_e represents the equilibrium concentration and q_e is the equilibrium adsorption capacity.

For the Langmuir isotherm model, the values of q_m and b can be calculated from the slope and intercept of plots of C_e/q_e vs. C_e, whereas the values of $1/n$ and K_F can be obtained by a plot of log q_e against C_e for the Freundlich isotherm model [42]. The adsorption parameters of the two isotherm models are shown in Table 3. The results revealed that Pb^{2+} adsorption onto the HAP and MHAPs were better fitted by the Langmuir model than the Freundlich model with higher correlation coefficients ($R^2 > 0.98$). The monolayer saturation adsorption capacity of MHAP calculated using the Langmuir model was 227.27 mg g^{-1}, which is more close to the experimental data.

Table 2
Comparison of the adsorption capacity for Pb^{2+} with reported adsorbents

Adsorbent	q_m (mg g^{-1})	Adsorption condition/ g+++	Reference
MHAP	218.0	C_0 = 550 mg L^{-1}, pH = 3.79, 30°C	This work
HAP	71.0	C_0 = 550 mg L^{-1}, pH = 3.79, 30°C	This work
HAP derived from gypsum waste	500	C_0 = 1,000 mg L^{-1}, pH = 5, 20°C	[12]
Calcined phosphate	85.6	C_0 = 100 mg L^{-1}, pH = 5, 20°C	[14]
Algae marine, nonliving biomass	126.5	C_0 = 500 mg L^{-1}, 50 mL, pH = 4.5, 30°C	[34]
Sepiolite	185.2	C_0 = 2,100 mg L^{-1}, 100 mL, 50°C	[35]
Fly ash-based geopolymer	182.4	C_0 = 140 mg L^{-1}, 50 mL, pH = 4, 45°C	[36]
Metakaolin-based geopolymer	100.0	C_0 = 300 mg L^{-1}, 50 mL, pH = 4, 25°C	[37]
Citric acid modified rubber leaf powder	109.9	C_0 = 100 mg L^{-1}, 50 mL, 25°C	[38]
Mesoporous silica-grafted graphene oxide (GO–SBA-15)	255.1	C_0 = 300 mg L^{-1}, 20 mL, pH = 5, 25°C	[39]
GO-HPEL gel	438.6	C_0 = 300 mg L^{-1}, 100 mL, pH = 5.8, 15°C	[40]
Magnetic Fe_3O_4-MnO_2 nanoplates	208.1	C_0 = 75 mg L^{-1}, 100 mL, pH = 6, 25°C	[41]

Table 3
Langmuir and Freundlich isotherm parameters for Pb^{2+} adsorption

Adsorbent	Langmuir model			Freundlich model		
	q_m/(mg/g)	K_L	R^2	K_F/(mg/g)(L/mg)$^{1/n}$	n	R^2
HAP	73.21	0.039	0.9880	25.42	6.15	0.9710
0.25MHAP	123.30	0.054	0.9936	29.28	4.06	0.9874
0.5MHAP	176.99	0.107	0.9979	34.94	3.09	0.9521
0.75MHAP	207.47	0.138	0.9934	62.72	4.35	0.8581
MHAP	227.27	0.228	0.9928	63.23	3.43	0.6496

The effect of temperature on the adsorption of Pb^{2+} by HAP and MHAP was also studied, as shown in Fig. 5 and Table S1. It was observed that a high temperature is beneficial for improving the adsorption capacity. As the temperature varied from 293 to 313 K, the adsorption capacity of HAP and MHAP increased from 67.6 to 82.0 mg g^{-1} and from 182.6 to 299.9 mg g^{-1}, respectively. This result was probably because the adsorption process was endothermic. The increase of temperature may increase the diffusion rate of Pb^{2+} across the external boundary layer and in the internal pores of the adsorbent, reduce the viscosity of the solution, and increase the number of active sites. To explore the adsorption thermodynamic process, the thermodynamic parameters, including the free energy change (ΔG), enthalpy change (ΔH) and entropy change (ΔS), were computed using the following equations:

$$\Delta G = \Delta H - T\Delta S \tag{4}$$

$$\Delta G = -RT\ln K_c \tag{5}$$

The equation is conveniently used in a linear form:

$$\ln K_c = -\frac{\Delta H}{RT} + \frac{\Delta S}{R} \tag{6}$$

where K_c is the equilibrium constant that is equal to the Langmuir constant b, R is the molar gas constant (8.314 J mol^{-1} K^{-1}) and T is the absolute temperature in Kelvin (K). The values of ΔS and ΔH can be calculated from the intercept and slope of a plot of $\ln K_c$ vs. $1/T$, and the results are presented in Table 4. The values of ΔH and ΔG were negative, which indicated that the process of adsorption for Pb^{2+} is spontaneous and endothermic. The value of ΔG for MHAP was larger than that for HAP, which suggested that the adsorption of Pb^{2+} was easier for MHAP. The randomness of the adsorption system for MHAP increased remarkably because the entropy change for MHAP was 243.13 J mol^{-1} K^{-1} and for HAP was 48.89 J mol^{-1} K^{-1}.

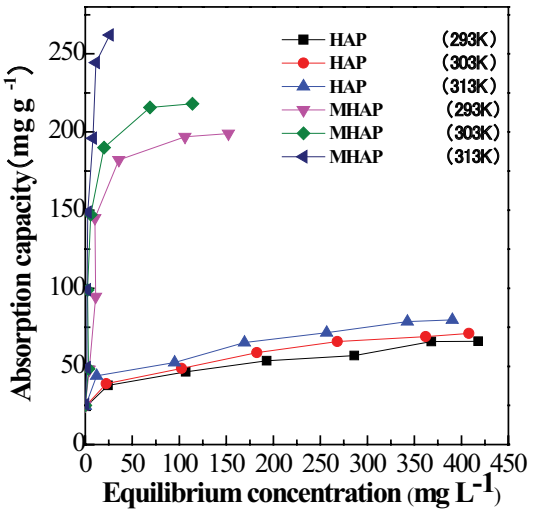

Fig. 5. Effect of temperature on the adsorption capacity of HAP and MHAP.

3.3. Adsorption kinetics and the effects of pH

The study of the adsorption kinetics can indicate the optimum operating conditions and reveal the adsorption reaction rate. Using concentrations of 200 and 500 mg L^{-1} as examples, the adsorption capacities of HAP and MHAP for Pb^{2+} as a function of the adsorption time are displayed in Fig. 6. Obviously, the kinetic curve of MHAP was similar to HAP, and the adsorption equilibrium time of both adsorbents was short. The adsorption process was roughly divided into two stages. In the first stage (t < 60 min), the rate of adsorption was rapid, especially during the initial

Table 4
Thermodynamic parameters for Pb^{2+} removal by HAP and MHAP

Adsorbent	R^2	ΔH (kJ mol^{-1})	ΔS (J mol^{-1} K^{-1})	ΔG (kJ mol^{-1})		
				293 K	303 K	313 K
HAP	0.9938	10.31	48.89	–4.01	–4.50	–4.99
MHAP	0.9523	63.17	243.13	–8.06	–10.50	–12.93

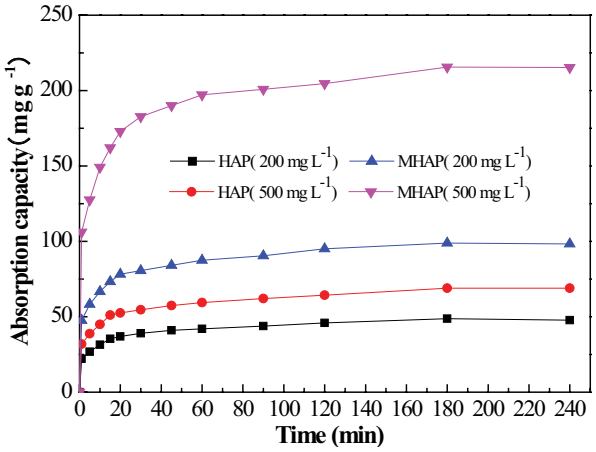

Fig. 6. Effect of the contact time on adsorption capacity of HAP and MHAP for Pb^{2+}.

20 min; 80% of the equilibrium adsorption capacity was achieved. In the second stage (60 min < t < 240 min), the adsorption capacity increased slightly as the time increased until the adsorption equilibrium was reached. Furthermore, with the increase in the aqueous lead concentration, the adsorption equilibrium time of MHAP did not increase. This result indicates that MHAP maintained a good adsorption kinetic performance for high lead concentrations.

The pseudo-first-order and pseudo-second-order models were used to describe the adsorption process. The expressions for the four kinetic models are shown in Eqs. (7) and (8):

$$\log\left(q_e - q_t\right) = \log q_e - \frac{k_1 t}{2.303} \tag{7}$$

$$\frac{t}{q_t} = \frac{1}{k_2 q_e^2} + \frac{t}{q_e} \tag{8}$$

where q_e and q_t (both in mg g^{-1}) are the amount of Pb^{2+} adsorbed per unit mass of the adsorbents at equilibrium and time t. k_1 and k_2 are the constants for the first-order-rate and second-order-rate models, respectively. The calculated parameters are presented in Fig. S3 and Table S2. It was obvious that the pseudo-second-order kinetic model with a high correlation coefficient (R^2 > 0.999) could better describe the behavior of Pb^{2+} adsorption on HAP and MHAP. In addition, the value of q_e^b (219.30 mg g^{-1}) calculated from the pseudo-second-order model was close to q_e^a (227.27 mg g^{-1}) that was estimated by the Langmuir isotherm model, which further illustrated the good fit of the pseudo-second-order kinetic model.

The effect of the solution pH on the removal of lead cannot be ignored. Suzuki et al. [43] reported that acidic conditions are suitable to remove Pb^{2+} for apatite. In this work, the effect of the pH from 2 to 6.5 on the adsorption of Pb^{2+} by HAP and MHAP was studied, as shown in Fig. S4. The results indicated that the removal of lead was almost unaffected by the pH value from pH 2 to 5.5 with a capacity of more than 200 mg g^{-1}. As the pH increased above 5.5, the amount of immobilized Pb^{2+} sharply increased, probably due to chemical precipitation of $Pb(OH)_2$ [44].

3.4. Mechanism of Pb^{2+} adsorption

To explore the mechanism of Pb^{2+} removal, the HAP and MHAP after adsorption of Pb^{2+} were analyzed using SEM, XPS and XRD. The SEM results (Fig. S5) showed some changes in the morphology, and some needle-like materials formed over the surface of the adsorbents after adsorption. The XPS spectra of MHAP before and after adsorption of Pb^{2+} are depicted in Fig. 7. There are two peaks in the spectra of Pb 4f, one at approximately 138.2 eV and the other at approximately 143.2 eV, which can be assigned to Pb $4f_{7/2}$ and Pb $4f_{5/2}$, respectively. However, no significant shifts or changes were observed in the spectra of Mg1s, P2p, and O1s after adsorption. The binding energies of the $P2p_{3/2}$ and O1s peaks were 132.4 and 531.0 eV, respectively, which coincided with the typical binding energy between P^{5+} and O-P with oxygen to form phosphate [45–47].

Fig. 8 shows the XRD patterns of MHAP and HAP after Pb^{2+} adsorption. The results demonstrated that the structure and composition of adsorbents significantly changed after adsorption. New compounds were formed, such as lead phosphate hydroxide ($Pb_5(PO_4)_3OH$, PDF-08-0259) or lead hydroxyapatite ($Pb_{10}(PO_4)_6(OH)_2$, PDF-# 51-1648) and calcium lead phosphate hydroxide ($Ca_2Pb_8(PO_4)_6(OH)_2$, PDF-# 40-1495). Clearly, the phosphate and hydroxyl were involved in the process of adsorption, and the removal of lead was mainly achieved by replacing Ca in HAP or Mg in MHAP.

Ma et al. [22] and Liu et al. [40] proposed that the reaction could be explained as ion–ion exchange if a value of approximately 1 was found for the molar ratio of $Mg_{release}/Pb_{adsorb}$ or $Ca_{release}/Pb_{adsorb}$. Fig. S6 presents the relationship of the molar ratios ($Mg_{release}/Pb_{adsorb}$ or $Ca_{release}/Pb_{adsorb}$) during Pb^{2+} immobilization. The results showed that the value of $Mg_{release}/Pb_{adsorb}$ was 0.9843 and 0.9743 for MHAP and HAP, respectively. From the stoichiometry, the dissolved calcium or magnesium showed an equal relationship with the amount of adsorbed lead. This phenomenon implied ion–ion exchange, and the corresponding equation is shown as Eq. (9). Lead adsorption by HAP based on ion–ion exchange should easily be achieved because of the crystalline structure of HAP. However, the removal of Pb^{2+} by adsorption on MHAP would better be explained by dissolution–precipitation than ion–ion exchange because the poor crystallization of MHAP results from destruction of the structure by Mg^{2+}. Dissolution–precipitation is a continuous process. The reaction of phosphate, hydroxyl and Pb^{2+} produced lead hydroxyapatite ($Pb_{10}(PO_4)_6(OH)_2$. Part of the Pb^{2+} could also precipitate with calcium, resulting in the formation of $Ca_{10-x}Pb_x(PO_4)_6(OH)_2$. The $Ca_{10-x}Pb_x(PO_4)_6(OH)_2$ crystals with a higher content of calcium were unstable [23] and could be dissolved, reacting with Pb^{2+} continuously until the formation of pure lead hydroxyapatite ($Pb_{10}(PO_4)_6(OH)_2$). The reaction equations are shown in Eqs. (10) and (11):

$$Ca_{10}\left(PO_4\right)_6\left(OH\right)_2 + xPb^{2+} \rightarrow Ca_{10-x}Pb_x\left(PO_4\right)_6\left(OH\right)_2 + xCa^{2+} \tag{9}$$

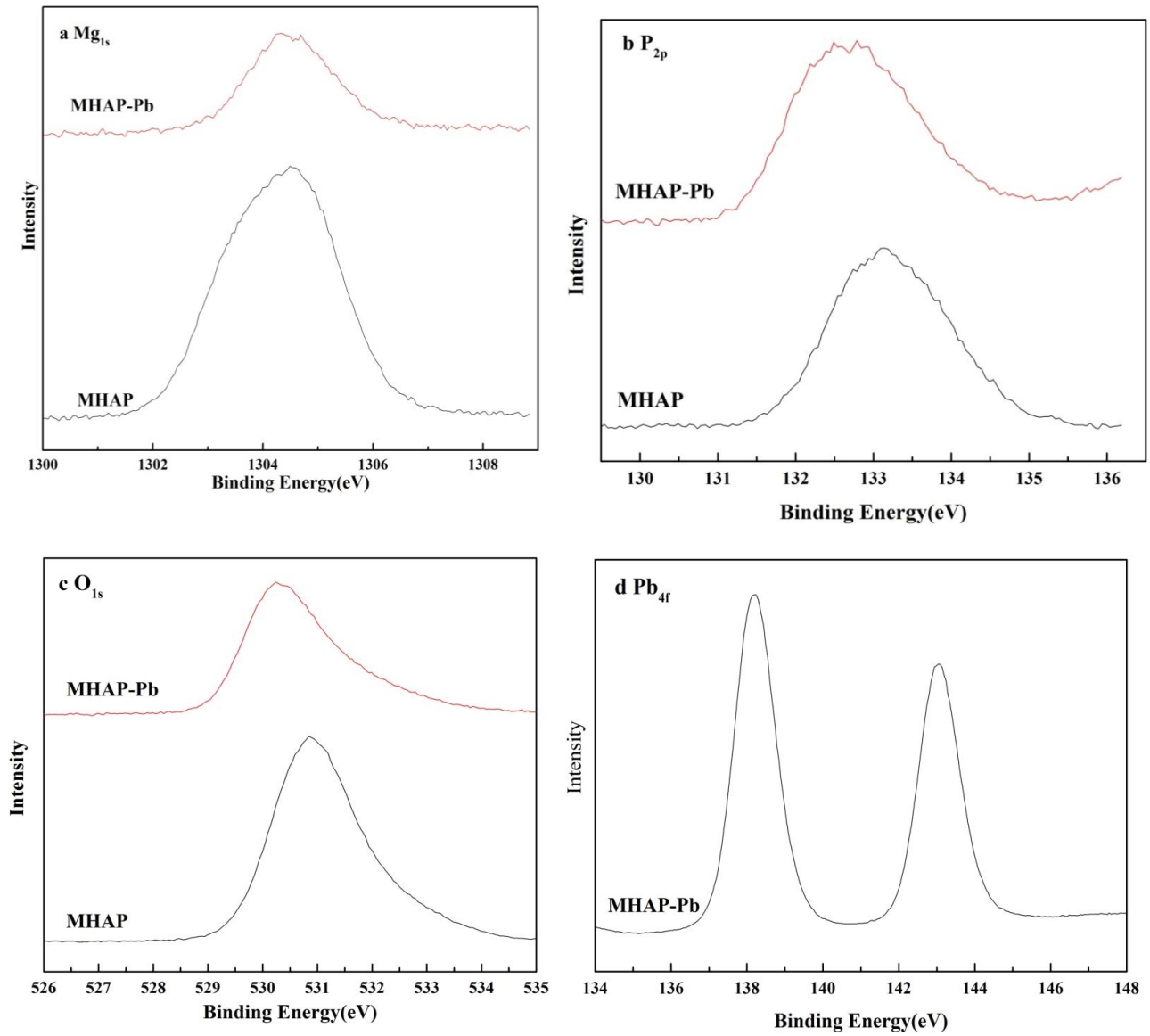

Fig. 7. XPS spectra of Mg1s (a), P2p (b), O1s (c) and Pb4f (d) of MHAP before and after Pb^{2+} adsorption.

$$\left(10-x\right)Ca^{2+}+xPb^{2+}+6PO_4^{3-}+2H_2O \Leftrightarrow Ca_{10-x}Pb_x\left(PO_4\right)_6\left(OH\right)_2+2H^+ \quad (10)$$

$$10Pb^{2+}6PO_4^{3-}+2H_2O \rightarrow Pb_{10}\left(PO_4\right)_6\left(OH\right)_2+2H^+ \quad (11)$$

The adsorption of Pb^{2+} by MHAP could be accomplished through two steps. The first step is the dissolution of phosphate and hydroxyl followed by the precipitation of Pb^{2+}. Therefore, increasing the dissolution of phosphate could improve the rate and extent of the precipitate formation and consequently enhance the adsorption rate and capacity of MHAP. However, the dissolution of the phosphate is closely related to the surface properties of the adsorbent. An adsorbent with a larger specific surface area and pore volume is more favorable in terms of dissolving the phosphate and hydroxyl groups. The number of PO_4^{3-} and –OH groups is a limiting factor in the formation of lead phosphate because the amount of Pb^{2+} is excessive. Increasing the number of surface PO_4^{3-} and –OH groups should be helpful for improving the rate and amount of lead phosphorus precipitate. Therefore, it could be concluded that the surface properties and number of functional groups of the adsorbent are the key factors for determining the adsorption capacity for Pb^{2+}. Compared with HAP, MHAP had a higher specific surface area and more surface functional groups, which explained its significantly larger adsorption capacity.

The lead hydroxyapatite crystallite possibly presents as a needle-like morphology, as shown in Fig. S5. Furthermore, lead phosphate ($Pb_9(PO_4)_6$, PDF-33-0768) was also detected with XRD (Fig. 8). Apart from calcium or magnesium substituted by lead, the phosphate group was also beneficial for removing aqueous Pb^{2+}. The reaction is described in Eq. (12):

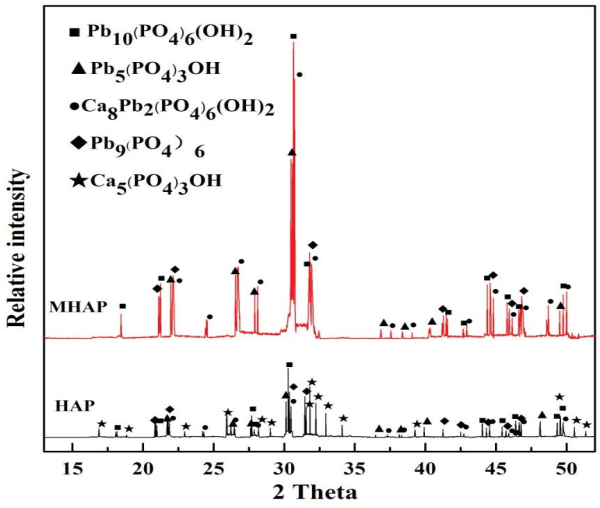

Fig. 8. XRD patterns of MHAP and HAP after Pb^{2+} adsorption.

$$9Pb^{2+} + 6PO_4^{3-} \rightarrow Pb_9\left(PO_4\right)_6 \quad (12)$$

In summary, the dissolution-precipitation mechanism was proposed as the predominant way in which Pb^{2+} is adsorbed onto MHAP. There were three patterns of Pb^{2+} immobilization: (1) incomplete substitution and formation of product similar to $Ca_2Pb_8(PO_4)_6(OH)_2$; (2) complete substitution to form $Pb_{10}(PO_4)_6(OH)_2$; and (3) PO_4^{3-} fixed with the free Pb^{2+} in an aqueous solution. Among them, the second method (i.e., complete substitution) showed the highest efficiency for removing Pb^{2+}.

4. Conclusions

In this work, magnesium-doped hydroxyapatite with a poor crystallinity was synthesized and used to adsorb Pb^{2+} from an aqueous solution. The equilibrium adsorption capacity was as high as 218 mg g^{-1} for MHAP at an initial Pb^{2+} concentration of 550 mg L^{-1}. The adsorption process was spontaneous and endothermic. The adsorption behavior of MHAP could be well explained by the Langmuir isotherm model and pseudo-second-order kinetic model. The adsorption mechanism was found to be the formation of Pb precipitates after the dissolution of apatite. Compared with HAP, the adsorption capacity of MHAP was significantly higher, which could be attributed to its larger specific surface area and more surface functional groups. This study demonstrated that MHAP is a potential adsorbent to remove lead contaminants from aqueous solutions.

Acknowledgments

This work was supported by the Natural Science Foundation of Jiangsu Province (No. BK20160241), National Natural Science Foundation of China (No. 51602344), National key R&D program of China (No. 2016YFE0102500) and the Priority Academic Program Development of Jiangsu Higher Education Institutions.

References

[1] M. Romano, H. Ferr eyra, G. Ferreyroa, F.V. Molina, A. Caselli, L. Barberis, P. Beldomenico, M. Uhart, Lead pollution from waterfowl hunting in wetlands and rice fields in Argentina, Sci. Total. Environ., 545 (2016) 104–113.
[2] N. Silva-Sánchez, J.E. Schofield, T.M. Mighall, A.M. Cortizas, K.J. Edwards, L. Foser, Climate changes, lead pollution and soil erosion in south Greenland over the past 700 years, Quaternary Res., 84 (2015) 159–173.
[3] U. Förstner, G.T.W. Wittmann, Metal Pollution in the Aquatic Environment, Springer, Berlin, Heidelberg, 1979.
[4] V.K. Gupta, S. Agarwal, T.A. Saleh, Synthesis and characterization of alumina-coated carbon nanotubes and their application for lead removal, J. Hazard. Mater., 185 (2011) 17–23.
[5] X. Huo, L. Peng, X. Xu, L. Zhang, B. Qiu, Z. Qi, Elevated blood lead levels of children in Guiyu, an electronic waste recycling town in China, Environ. Health Persp., 115 (2007) 1113–1117.
[6] J. Liu, Y. Ai, L. McCauley, J.P. Martin, C.H. Yan, X.M. Shen, H. Needleman, Blood lead levels and associated sociodemographic factors among preschool children in the South Eastern region of China, Paediatr. Perinat, EP, 26 (2012) 61–69.
[7] Z. Elouear, J. Bouzid, N. Boujelben, M. Feki, F. Jamoussi, A. Montiel, Heavy metal removal from aqueous solutions by activated phosphate rock, J. Hazard. Mater., 156 (2008) 412–420.
[8] M.K. Uddin, A review on the adsorption of heavy metals by clay minerals, with special focus on the past decade, Chem. Eng. J., 308 (2017) 438–462.
[9] O. Kaygili, S.V. Dorozhkin, T. Ates, A.A. Al-Ghamdi, F. Yakuphanoglu, Dielectric properties of Fe doped hydroxyapatite prepared by sol–gel method, Ceram. Int., 40 (2014) 9395–9402.
[10] Y. Feng, J.L. Gong, G.M. Zeng, Q.Y. Niu, H.Y. Zhang, C.G. Niu, J.H. Deng, M. Yan, Adsorption of Cd (II) and Zn (II) from aqueous solutions using magnetic hydroxyapatite nanoparticles as adsorbents, Chem. Eng. J., 162 (2010) 487–494.
[11] L. Cui, Y. Wang, L. Hu, L. Gao, B. Du, Q. Wei, Mechanism of Pb (II) and methylene blue adsorption onto magnetic carbonate hydroxyapatite/graphene oxide, RSC Adv., 5 (2015) 9759–9770.
[12] Y. Hashimoto, T. Sato, Removal of aqueous lead by poorly-crystalline hydroxyapatites, Chemosphere, 69 (2007) 1775–1782.
[13] F. Fernane, S. Boudia, F. Aiouache, Removal Cu (II) and Ni (II) by natural and synthetic hydroxyapatites: a comparative study, Desal. Wat. Treat., 52 (2014) 2856–2862.
[14] X.Y. Zhao, Y.J. Zhu, J. Zhao, B.Q. Lu, F. Chen, C. Qi, J. Wu, Hydroxyapatite nanosheet-assembled microspheres: hemoglobin-templated synthesis and adsorption for heavy metal ions, J. Colloid Interface Sci., 416 (2014) 11–18.
[15] S. Hokkanen, E. Repo, L.J. Westholm, S. Lou, T. Sainio, M. Sillanpää, Adsorption of Ni^{2+}, Cd^{2+}, PO_4^{3-} and NO^{3-} from aqueous solutions by nanostructured microfibrillated cellulose modified with carbonated hydroxyapatite, Chem. Eng. J., 252 (2014) 64–74.
[16] G. Udhayakumar, N. Muthukumarasamy, D. Velauthapillai, S.B. Santhoshh, A. Vijayshankar, Magnesium incorporated hydroxyapatite nanoparticles: preparation, characterization, antibacterial and larvicidal activity, Arab. J. Chem., 11 (2018) 645–654.
[17] J.R. Ramya, K.T. Arul, K. Elayaraja, S.N. Kalkura, Physicochemical and biological properties of iron and zinc ions co-doped nanocrystalline hydroxyapatite, synthesized by ultrasonication, Ceram. Int., 40 (2014) 16707–16717.
[18] Y. Nie, C. Hu, C. Kong, Enhanced fluoride adsorption using Al (III) modified calcium hydroxyapatite, J. Hazard. Mater., 233 (2012) 194–199.
[19] L. Chen, K.S. Zhang, J.Y. He, X.J. Huang, J.H. Liu, Enhanced fluoride removal from water by sulfate-doped hydroxyapatite hierarchical hollow microspheres, Chem. Eng. J., 285 (2016) 616–624.
[20] T. Suzuki, T. Hatsushika, M. Miyake, Synthetic hydroxyapatites as inorganic cation exchangers. Part 2, J. Chem. Soc., Faraday Trans., 78 (1982) 3605–3611.

[21] F. Fernane, M.O. Mecherri, P. Sharrock, M. Fiallo, R. Sipos, Hydroxyapatite interactions with copper complexes, Mater. Sci. Eng. C, 30 (2010) 1060–1064.
[22] Q.Y. Ma, S.J. Traina, T.J. Logan, In situ lead immobilization by apatite. Environ. Sci. Technol., 27 (1993) 1803–1810.
[23] Y. Xu, F.W. Schwartz, Lead immobilization by hydroxyapatite in aqueous solutions, J. Contam. Hydrol., 15 (1994) 187–206.
[24] E. Mavropoulos, A.M. Rossi, A.M. Costa, Studies on the mechanisms of lead immobilization by hydroxyapatite, Environ. Sci. Technol., 36 (2002) 1625–1629.
[25] L.P. Higuita, A.F. Vargas, M.J. Gil, L.F. Giraldo, Synthesis and characterization of nanocomposite based on hydroxyapatite and monetite, Mater. Lett., 175 (2016) 169–172.
[26] E. Ahmadzadeh, F. Talebnia, M. Tabatabaei, H. Ahmadzadeh, B. Mostaghaci, Osteoconductive composite graft based on bacterial synthesized hydroxyapatite nanoparticles doped with different ions: from synthesis to in vivo studies, Nanomed-nanotechnol., 12 (2016) 1387–1395.
[27] H.B. Lu, C.T. Campbell, D.J. Graham, B.D. Ratner, Surface characterization of hydroxyapatite and related calcium phosphates by XPS and TOF-SIMS, Anal. Chem., 72 (2000) 2886–2894.
[28] S. Chander, D.W. Fuerstenau, An XPS study of the flouride uptake by hydroxyapatite, Colloids Surf., 13 (1985) 137–144.
[29] K. Nagakane, Y. Yoshida, I. Hirata, R. Fukuda, Y. Nakayama, K. Shirai, T. Ogawa, K. Suzuki, B.V. Meerbeek, M. Okazaki, Analysis of chemical interaction of 4-MET with hydroxyapatite using XPS, Dent. Mater. J., 25 (2006) 645–649.
[30] Y.J. Wang, J.H. Chen, Y.X. Cui, S.Q. Wang, D.M. Zhou, Effects of low-molecular-weight organic acids on Cu (II) adsorption onto hydroxyapatite nanoparticles, J. Hazard. Mater., 162 (2009) 1135–1140.
[31] N. Ohtsu, S. Hiromoto, M. Yamane, K. Satoh, M. Tomozawa, Chemical and crystallographic characterizations of hydroxyapatite- and octacalcium phosphate-coatings on magnesium synthesized by chemical solution deposition using XPS and XRD, Surf. Coat. Technol., 218 (2013) 114–118.
[32] R.M. Wilson, J.C. Elliott, S.E.P. Dowker, L.M. Rodriguez-Lorenzoc, Rietveld refinements and spectroscopic studies of the structure of Ca-deficient apatite, Biomaterials, 26 (2005) 1317–1327.
[33] Z.S. Tao, W.S. Zhou, X.W. He, W. Liu, B.L. Bai, Q. Zhou, Z. L. Huang, K. Tu, H. Li, T. Sun, Y. X. Lv, W. Cui, L. Yang, A comparative study of zinc, magnesium, strontium incorporated hydroxyapatite-coated titanium implants for osseointegration of osteopenic rats, Mater. Sci. Eng. C, 62 (2016) 226–232.
[34] R. Jalali, H. Ghafourian, Y. Asef, S.J. Davapanah, S. Sepehr, Removal and recovery of lead using nonliving biomass of marine algae, J. Hazard. Mater., 92 (2002) 253–262.
[35] N. Bektaş, B.A. Ağım, S. Kara, Kinetic and equilibrium studies in removing lead ions from aqueous solutions by natural sepiolite, J. Hazard. Mater., 112 (2004) 115–122.
[36] K. Al-Zboon, M.S. Al-Harahsheh, F.B. Hani, Fly ash-based geopolymer for Pb removal from aqueous solution, J. Hazard. Mater., 188 (2011) 414–421.
[37] T.W. Cheng, M.L. Lee, M.S. Ko, T.H. Ueng, S.F. Yang, The heavy metal adsorption characteristics on metakaolin-based geopolymer, Appl. Clay Sci., 56 (2012) 90–96.
[38] F. Fadzil, S. Ibrahim, M.A.K.M. Hanafiah, Adsorption of lead (II) onto organic acid modified rubber leaf powder: batch and column studies, Process Saf. Environ., 100 (2016) 1–8.
[39] X.H. Li, Z. Wang, Q. Li, J.X. Ma, M.Z. Zhu, Preparation, characterization, and application of mesoporous silica-grafted graphene oxide for highly selective lead adsorption, Chem. Eng. J., 273 (2015) 630–637.
[40] Y. Liu, L. Xu, J. Liu, J.S. Liu, X.Y. Liu, C.H. Chen, G.Y. Li, Y.F. Meng, Graphene oxides cross-linked with hyperbranched polyethylenimines: preparation, characterization and their potential as recyclable and highly efficient adsorption materials for lead (II) ions, Chem. Eng. J., 285 (2016) 698–708.
[41] J. Zhao, J. Liu, N. Li, W. Wang, J. Nan, Z.W. Zhao, F.Y. Cui, Highly efficient removal of bivalent heavy metals from aqueous systems by magnetic porous Fe_3O_4-MnO_2: Adsorption behavior and process study, Chem. Eng. J., 304 (2016) 737–746.
[42] M.E. Mahmoud, G.M. Nabil, N.M. El-Mallah, H.I. Bassiouny, S. Kumar, T.M. Abdel-Fattah, Kinetics, isotherm, and thermodynamic studies of the adsorption of reactive red 195 A dye from water by modified Switchgrass Biochar adsorbent, J. Ind. Eng. Chem., 37 (2016) 156–167.
[43] T. Suzuki, K. Ishigaki, M. Miyake, Synthetic hydroxyapatites as inorganic cation exchangers Part 3-Exchange characteristics of lead ions (Pb^{2+}), J. Chem. Soc., Faraday Trans., 80 (1984) 3157–3165.
[44] X. Cao, L.Q. Ma, D.R. Rhue, C.S. Appel, Mechanisms of lead, copper, and zinc retention by phosphate rock, Environ. Pollut., 131 (2004) 435–444.
[45] T.F. Stoica, C. Morosanu, A. Slav, T. Stoica, P. Osiceanu, C. Anastasescu, M. Gartner, M. Zaharescu, Hydroxyapatite films obtained by sol–gel and sputtering, Thin Solid Films, 516 (2008) 8112–8116.
[46] S. Kačiulis, G. Mattogno, L. Pandolfi, M. Cavalli, G. Gnappi, A. Montenero, XPS study of apatite-based coatings prepared by sol–gel technique, Appl. Surf. Sci., 151 (1999) 1–5.
[47] N. Ohtsu, Y. Nakamura, S. Semboshi, Thin hydroxyapatite coating on titanium fabricated by chemical coating process using calcium phosphate slurry, Surf. Coat. Technol., 206 (2012) 2616–2621.

Supplementary information:

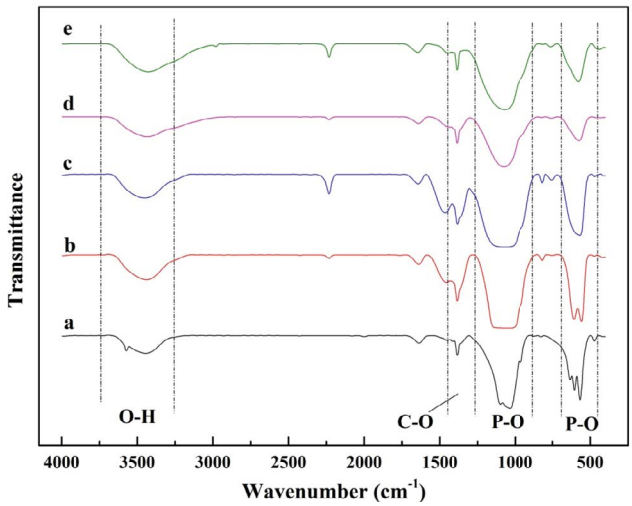

Fig. S1. FT-IR spectra of HAP (a), 0.25 MHAP (b), 0.5 MHAP (c), 0.75 MHAP (d) and MHAP (e).

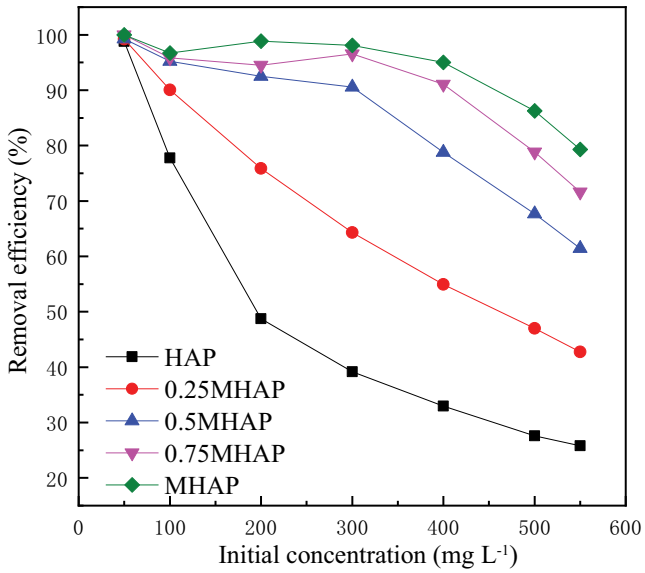

Fig. S2. Removal efficiency for Pb^{2+} by HAP, 0.25 MHAP, 0.5 MHAP, 0.75 MHAP and MHAP samples at different initial concentrations and 303 K.

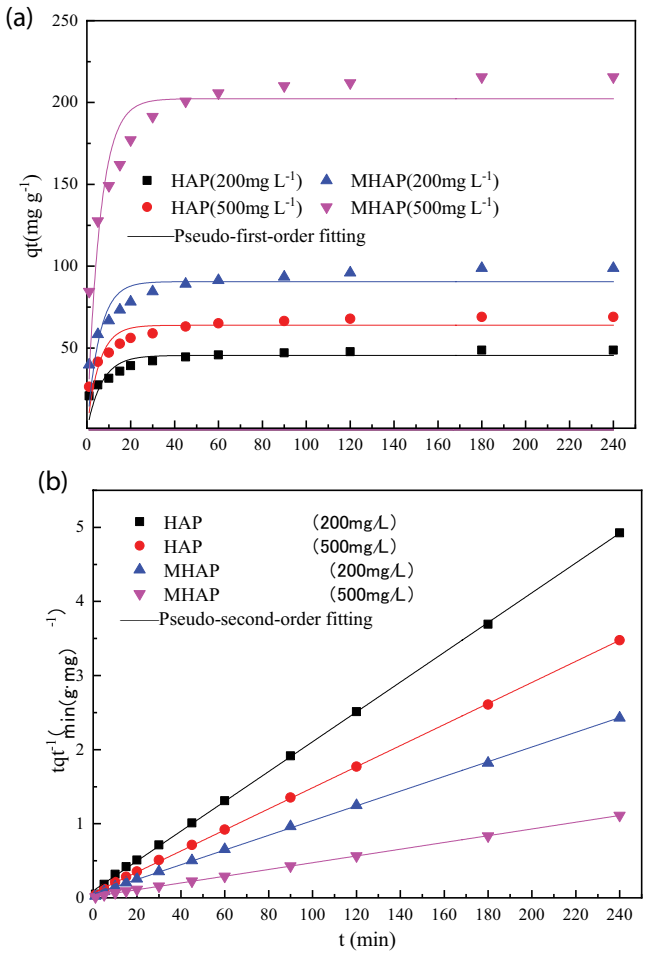

Fig. S3. Fitting of kinetic data with the pseudo-first-order kinetic model and pseudo-second-order kinetic model.

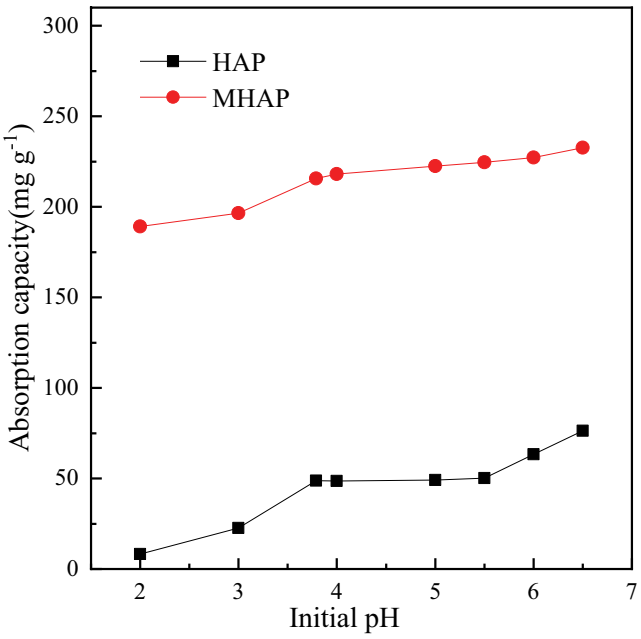

Fig. S4. Effect of initial pH on adsorption capacity of HAP and MHAP for Pb^{2+}

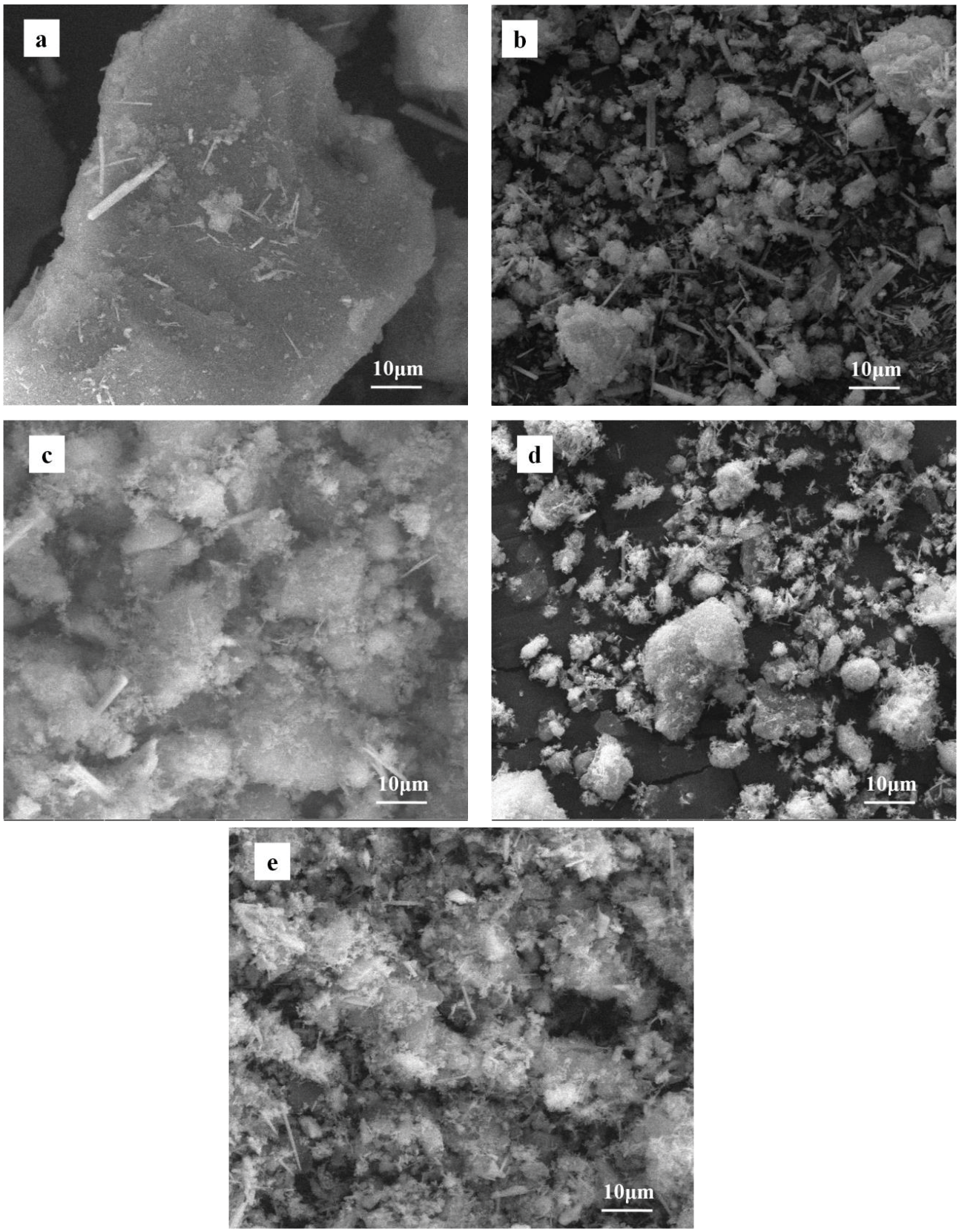

Fig. S5. SEM images of HAP (a), 0.25 MHAP (b), 0.5 MHAP (c), 0.75 MHAP (d) and MHAP (e) after lead adsorption.

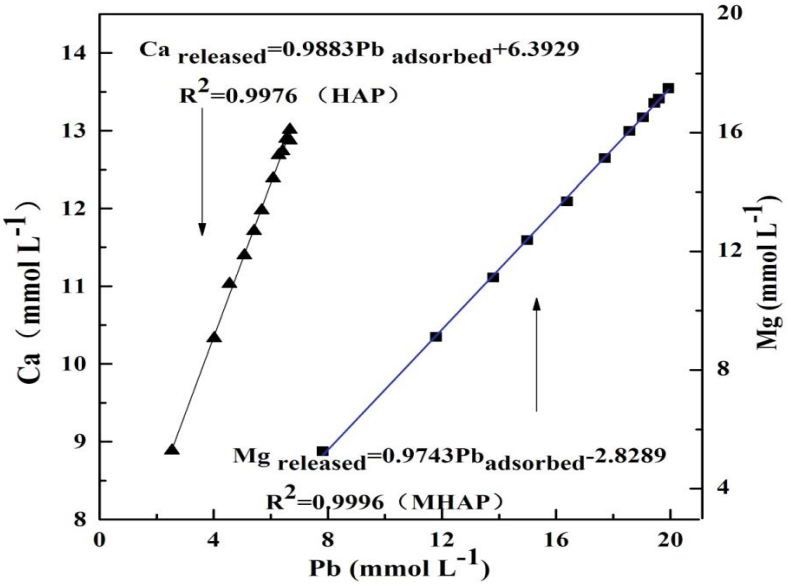

Fig. S6. Change in the released Ca^{2+} and adsorbed Mg^{2+} in solution (T = 30°C, initial pH = 3.79).

Table S1
Langmuir and Freundlich isotherm parameters for Pb^{2+} adsorption at different temperature

Adsorbent	Temperature (K)	Langmuir model			Freundlich model		
		q_m/(mg g^{-1})	K_L	R^2	K_F/(mg g^{-1})(L/mg)$^{1/n}$	n	R^2
HAP	293	67.66	0.036	0.9818	23.04	6.0	0.9773
	303	73.21	0.039	0.9880	25.42	6.15	0.9710
	313	81.77	0.042	0.9836	28.68	6.13	0.9749
MHAP	293	209.64	0.134	0.9932	62.76	4.34	0.8587
	303	227.27	0.228	0.9928	63.23	3.43	0.6496
	313	300.30	0.270	0.9263	62.31	1.97	0.7668

Table S2
Adsorption kinetic parameters for Pb^{2+} adsorption with different model (303 K)

Adsorbent	$q_{e,exp}$/(mg/g)	C_o/(mg/L)	Pseudo-first-order kinetic model			Pseudo-second-order kinetic model		
			k_1/min^{-1}	$q_{e,cal}$/(mg/g)	R^2	k_2/min^{-1}	$q_{e,cal}$/(mg/g)	R^2
HAP	73.21	200	0.34	45.47	0.6361	0.0042	49.73	0.9997
		500	0.41	63.9	0.7175	0.0032	70.32	0.9998
MHAP	227.27	200	0.40	90.56	0.6595	0.0020	100.70	0.9996
		500	0.39	202.31	0.7223	0.0011	219.30	0.9998